High Performance Chromatographic Characterization of Surface Chemical Heterogeneities of Fluorescent Organic-Inorganic Hybrid Core-Shell Silica Nanoparticles

Thomas C. Gardinier[#1], **Ferdinand F.E. Kohle**[#2], **James S. Peerless**[3], **Kai Ma**[1], **Melik Z. Turker**[1], **Joshua A. Hinckley**[2], **Yaroslava G. Yingling**[3], and **Ulrich Wiesner**[1,2,*]

[1]Materials Science and Engineering, Cornell University, Ithaca, NY 14853, USA

[2]Chemistry and Chemical Biology, Cornell University, Ithaca, NY 14853, USA

[3]Materials Science and Engineering, North Carolina State University, Raleigh, NC 27606, USA

[#] These authors contributed equally to this work.

Abstract

In contrast to small molar mass compounds, detailed structural investigations of inorganic core-organic ligand shell hybrid nanoparticles remain challenging. Assessment of batch reaction induced heterogeneities of surface chemical properties and their correlation with particle size has been a particularly long-standing issue. Applying a combination of high performance liquid chromatography (HPLC) and gel permeation chromatography (GPC) to ultrasmall (< 10 nm diameter) poly(ethylene glycol) coated (PEGylated) fluorescent core-shell silica nanoparticles, here we elucidate previously unknown surface heterogeneities resulting from varying dye conjugation to nanoparticle silica cores and surfaces. Heterogeneities are predominantly governed by dye charge as corroborated by molecular dynamics simulations. We demonstrate that this insight enables development of synthesis protocols to achieve PEGylated and targeting ligand functionalized PEGylated silica nanoparticles with dramatically improved surface chemical homogeneity as evidenced by single peak HPLC chromatograms. Since surface chemical properties are key to all nanoparticle interactions, we expect these methods and fundamental insights to become relevant to a number of systems for applications including bioimaging and nanomedicine.
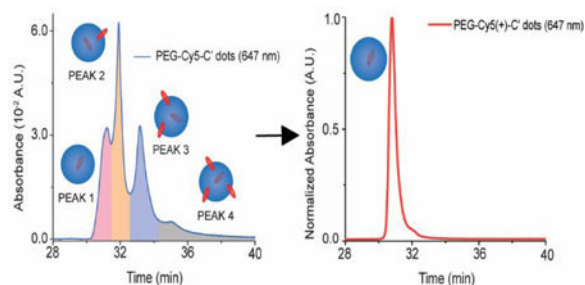
Table of Contents Graphic:

Keywords

nanoparticles heterogeneity; nanoparticle characterization; surface chemistry heterogeneity; nanoparticle surface functionalization; high performance liquid chromatography; fluorescence correlation spectroscopy; molecular dynamics

The study of ultrasmall (<10 nm diameter) nanoparticles (NPs) is an area of rapidly growing academic and technological interest as a result of size dependent properties and applications ranging from catalysis to nanomedicine. [1–3] While in the past decade the library of ultrasmall NPs has expanded substantially, detailed characterization of heterogeneities in surface−chemical composition has remained challenging. Biological nanomaterials such as proteins, antibodies, and their fragments have the advantage of consistent molar mass, and are now routinely analyzed by techniques such as high performance liquid chromatography (HPLC) and liquid chromatography coupled mass spectrometry (LC-MS).[4–6] In contrast, single-batch ultrasmall synthetic hybrid NPs often composed of inorganic cores and organic ligand shells typically display a distribution of sizes, masses, and surface chemistries that is not well characterized,[7,8] despite being of paramount importance, *e.g.* for the therapeutic and diagnostic application of nanomaterials.[9–11]

Here we turn to a combination of HPLC and gel permeation chromatography (GPC) for ultrasmall core−shell NP assessment. While the use in particular of HPLC for the characterization of organic compounds and macromolecules is ubiquitous,[12] its application to organic-inorganic hybrid NPs is scarce.[8] Employing fluorescent silica core-poly(ethylene glycol) (PEG) shell hybrid NPs referred to as Cornell dots or simply C dots with diameters below 10 nm,[13,14] we show that the extreme sensitivity of HPLC to small changes in chemistry provides insights into surface-chemical heterogeneity and its control. In combination with other techniques, including single molecule photo-bleaching experiments, fluorescence correlation spectroscopy (FCS), and molecular dynamics (MD) simulations, we elucidate the molecular origin of these heterogeneities and correlate them to particle size *via* coupled GPC−HPLC runs. Finally, based on these insights we develop synthesis protocols for PEGylated and targeting ligand functionalized PEGylated C dots with single peak HPLC chromatograms, *i.e.* with minimal heterogeneities in surface chemical properties. We expect that our methods and insights will be applicable to other ultrasmall core−shell hybrid NP systems and will enable synthesis of better defined materials for applications, *e.g.* in bioimaging and nanomedicine.

Results

We focused on fluorescent Cy5 dye encapsulating poly(ethylene glycol) coated (PEGylated) particles synthesized in water referred to PEG-Cy5-C' dots (C prime dots) and cyclic targeting peptide, c(RGDyC), functionalized c(RGDyC)-PEG-Cy5-C' dots.[15,16] While a first human clinical trial with such NPs suggested their safety,[3] future high-dose therapeutic applications of this and similar NP systems would tremendously benefit from high-resolution chromatographic characterization, which is standard for conventional pharmaceutical products. After synthesis, C' dot batches were subjected to GPC purification removing impurities including particle aggregates, free dye, and free PEG/c(RGDyC)-PEG resulting in single-peak chromatograms as shown for PEG-Cy5-C' dots in Fig. 1A.[17] Purified C' dots were subsequently characterized using an HPLC method tuned to separate NPs based on variations in surface chemical properties (see Methods). A representative HPLC chromatogram for PEG-Cy5-C' dots as detected at the 647 nm Cy5 absorbance wavelength (Fig. 1B, blue line) surprisingly revealed four distinct features, three dominant peaks <34 min and a small peak ~35 min. Using a 275 nm detector sensitive to PEG, the chromatogram reproduced the three dominant peaks, albeit with different intensities (Fig. 1B, red line). The corresponding HPLC chromatogram for the c(RGDyC)-PEG-Cy5-C' dots (Fig. 1C) was less well resolved due to peak broadening, but the main features of the PEG-Cy5-C' dot chromatogram were still present. This suggested that the main source of heterogeneity as detected by our HPLC method was not the targeting peptides, but associated with the PEG-Cy5-C' dot synthesis.[3,18]

Cross experiments identified the origin of these heterogeneities. First, we synthesized same size PEG-C' dots without Cy5 dye. Our HPLC method with 275 nm detection revealed a single peak at the position of the first peak observed for PEG-Cy5-C' dots (Fig. 1B, black line), suggesting its assignment to a particle fraction with the same surface characteristics as the PEG- C' dots, *i.e.* a purely PEGylated silica surface.[8] These particles may or may not contain a dye. If they do, it must be fully encapsulated within the silica core (see illustration in Figure 1D inset). Results therefore suggested Cy5 dye encapsulation chemistry as the source of the heterogeneities.

Photobleaching offers insights into HPLC Results

We next immobilized biotin-functionalized PEG-Cy5-C' dots on glass slides previously functionalized with streptavidin (Fig. 2A) for exposure to the evanescence field of a fluorescence microscope in total internal reflection geometry at low laser power and in the presence of an oxygen scavenger system (see Methods section). Continuous exposure caused Cy5 dye photobleaching. Image stacks were recorded until 99% of the original fluorescence signal was muted (Fig. 2B). Representative fluorescence time traces were extracted from the images (Fig. 2C). When a dye bleaches, a sharp step in the intensity trace is observed (orange arrows). The traces show NPs with one, two, three, and four steps, respectively, before the intensity reaches the background, suggesting one to four dyes per particle. About 650 immobilized NPs of a single synthesis batch were analyzed. The resulting statistics (Fig. 2D) indicated that ~55% of the dots had one dye, with increasingly smaller numbers of NPs carrying two, three, or four dye molecules per particle, respectively. Together with the HPLC

results this led us to the hypothesis that the four HPLC peaks are associated with zero, one, two, or three Cy5 dyes, respectively, positioned at the silica core surface.

FCS coupled with HPLC characterization of batch reaction particles

Cyanine dyes like Cy5 undergo photo-induced cis-trans isomerization around the polymethine bridge between a fluorescent trans-state and a non-fluorescent cis-state.[19] The associated rates are sensitive to the steric environment, have been used to probe membrane micro-viscosity of cells,[19,20] and can be observed in fluorescence correlation spectroscopy (FCS) at short lag times ($<10^{-5}$ s) by a change of the amplitude in the correlation curve, as well as a change of associated characteristic relaxation time.[19] We compared FCS measurements on HPLC fractions associated with each of the three dominant peaks 1–3 (Fig. 2E) as well as with unfractioned particles and free Cy5 dye. Particle FCS curves are shifted to longer times relative to free dye due to larger size. Isolated contributions of cis-trans photo-isomerization to the respective FCS curves are shown in (ii). From FCS, all NPs had the same size (inset of Fig. 2E and Fig. 2F) confirming that HPLC is separating peaks predominantly as a function of particle surface chemistry. This is corroborated by additional transmission electron microscopy (TEM) images of fractions of the particles corresponding to the different HPLC peaks 1–4 in Fig.1B/D exhibiting no substantial or systematic differences between fractions (see Supporting Information Figure S1), and silica core diameters between 3 and 4 nm, also consistent with previous work.[15,16] Fractions showed increasing numbers of dyes per particle as elution time increased (Fig. 2H), corroborating that additional dye on the particle surface is the source of the heterogeneity. From Fig. 2G, brightness per dye decreases with increasing peak elution time,[21] consistent with energy transfer between dyes or near surface dye locations. With a Cy5 hydrodynamic diameter of roughly 1.3 nm (Fig. 2H), two or more dyes may not fully reside inside a silica NP core of only 2.5 nm hydrodynamic radius. Dyes on the NP surface are less confined than dyes fully encapsulated within the rigid silica matrix and may be prone to additional forms of non-radiative energy dissipation.[21] One of those for Cy5 is photo-isomerization, which we analyzed for each HPLC fraction as compared to unfractionated PEG-Cy5-C' dots. As peak elution time increases, the percentage of dye undergoing photo-isomerization increases (Fig. 2I), suggesting that particles with larger dye numbers are likely to have more Cy5 molecules on the particle surface, consistent with our hypothesis. The sensitivity of the HPLC method is so high, that the difference of one dye on the silica core surface will have significant effects on elution time. We estimated the percentage of particles with zero, one, two, or three dyes on the surface from HPLC peak area integrations (Supporting Information, Table S5). Differences to results from the dye photobleaching statistics (Fig. 2D) can be rationalized by the fact that HPLC does not separate based on the absolute number of dyes per particle, which includes particles that have dyes on the surface and fully encapsulated in the core.

Using coupled GPC-HPLC to elucidate size dependence of surface chemistry

To elucidate variations in surface chemical properties as a function of particle size within a particle synthesis batch expected to have substantial impact, *e.g.* on biological properties of NPs,[22,23] we performed coupled GPC-HPLC separations. A sample of pre-purified PEG-Cy5-C' dots was split into 15 fractions using GPC, which were then linearly up-concentrated to retain their GPC concentration relationship (inset Fig. 3A) and sequentially

injected into the HPLC. Results are plotted in two-dimensional (2D waterfall) plots with HPLC and GPC resolution along the x and y axes, respectively, and absorbance along the z axis (Fig. 3). Concentration differences between tailing and central GPC fractions caused loss of full peak resolution for the tailing fractions (Fig. 3A). This could be circumvented by moving to a subset of eight GPC fractions, each adjusted to the same final concentration and run through the HPLC (Fig. 3B and inset), exhibiting no substantial dependence of the surface chemical properties on particle size. Detailed comparison of fractions 13, 16, and 20 representing large, medium, and small NPs of the distribution, respectively, reveal a small increase in surface bound dyes with NP size as expected from their increased surface area (Fig. 3D). For these PEG-Cy5-C' dot batches fear of the "worst-case scenario", with surface chemical properties strongly correlated with size, and thus maximum complexity in particle heterogeneity, is unsubstantiated.

Control of surface chemistry heterogeneity through electrostatics

In an effort to control particle heterogeneity, HPLC results were evaluated as a function of dye chemistry/charge. In addition to working with negatively charged Cy5, we synthesized PEG-C' dots from zwitterionic TMR and positively charged ATTO647N dyes (Fig. 4). We used GPC on native synthesis solutions to monitor dye incorporation efficiency and HPLC on GPC purified samples to characterize surface chemical properties. Dye incorporation efficiency and homogeneity of surface chemical properties substantially increased in the sequence Cy5 < TMR < ATTO647N (Fig. 4A-F), with ATTO647N resulting in single peak chromatograms for both GPC and HPLC (Fig. 4C and F). Incorporation efficiencies were near 100% for ATTO647N, 82% for TMR, and only 62% for Cy5 (Supporting Information Fig. S4-S6 and Tables S2-S). Net dye charge plays a crucial role in both efficient dye encapsulation in silica and heterogeneity of surface chemical properties. Results can be rationalized by considering Coulomb interactions between dye and silica NPs during growth: At our basic synthesis conditions silica NPs are far above their isoelectric point (pH~2–3) and are stabilized by negative surface charges before surface PEGylation[16]. Interactions therefore switch from repulsive to attractive when moving from Cy5 across TMR to ATTO647N, consistent with increasing dye incorporation efficiency as revealed by GPC, numbers of dyes per particle for the latter two as determined by FCS (Supporting Information, Table S1 and Fig. S2-S3), and improved homogeneity of surface chemical properties as documented by HPLC.

Trends were primarily dependent on dye charge and not on specific dye chemical characteristics as revealed by substituting Cy5, TMR, and ATTO647N with same net charge series Cy3, ATTO680, and weakly fluorescent dye MB2, respectively. Despite slight differences, *e.g.* in HPLC retention time between PEG-ATTO647N-C' dots and PEG-MB2-C' dots (compare Fig. 4F and I) or in peak width between PEG-TMR-C' dots and PEG-ATTO680-C' dots (compare Fig. 4E and H), this series (Fig. 4G to I) matches the overall peak structure of the earlier series well with negatively charged Cy3 dye (like Cy5 dye) producing 4 peaks and positively charged MB2 dye (like ATTO647N dye) resulting in essentially a single relatively sharp peak.

Comparing data in Figure 4D to 4I, the highest degree of particle homogeneity in surface chemical properties was obtained for PEG-MB2-C' dots (see Fig. 4I). For a synthesis batch of these particles we conducted coupled GPC-HPLC experiments. PEG-MB2-C' dots fractionated with GPC, normalized in concentration, and subjected to HPLC, revealed no substantial dependence of the surface chemical acknproperties on particle size (Fig. 3C and inset). Detailed comparison of different fractions revealed a small increase in surface bound dyes as particle size decreases (Fig. 3F). Overall, results corroborated earlier conclusions for PEG-Cy5-C' dots that for this synthesis approach to fluorescent core-shell silica NPs, heterogeneities in particle size and surface chemical properties are essentially uncorrelated. Comparison of waterfall plots in Figure 3B and C for PEG-Cy5-C' dots and PEG-MB2-C' dots demonstrates substantial improvement in particle batch surface chemical homogeneity achieved by the appropriate choice of dye.

Molecular dynamics simulations provide insights into mechanism of dye encapsulation

The origin of the observed differences in dye incorporation efficiency and dye location either on the surface or in the NP core was elucidated by all-atom MD simulations.[24,25] Atomistic MD has been extensively employed to study silica surfaces and their interactions with silanes and other organics.[26–29] We constructed systems (see Methods) of amorphous silica with a given surface charge (ratio of $SiO^-/SiOH$ units available on the surface referred to as the deprotonation percentage), a single dye molecule, water, and the number of ammonium ions necessary to reach a net-neutral system charge (Fig. 5A, for dimensions see Supporting Information, Fig. S8). The resulting total non-bonded interaction energies between the silica surfaces and the dye silanes over the last 20 ns of the production simulations are shown in Fig. 5B where large negative values indicate strong attraction, whereas positive values indicate repulsion (Supporting Information, Fig. S9). All three dyes have a similarly strong affinity to the passivated surface of a fully-formed nanoparticle (with Cy5 potentially being slightly more attracted) as represented by the 1% deprotonated surface. A more-negatively-charged 15% deprotonated surface, representative of intermediate silica cluster surfaces during synthesis, shows unchanged affinity for TMR and ATTO647N. In contrast, Cy5 shows little to slightly repulsive interaction, suggesting that Cy5 is less attracted to these clusters and therefore less likely to be incorporated into the core of the particle. These varying results as a function of the deprotonation percentage not only rationalize why negatively charged Cy5 is not incorporated in the inside of the silica core, but also why it ends up on the core surface. Moreover, analyzing the interaction energies between specific atomic groups within the dye molecules and the silica surface (Supporting Information, Fig. S10) provides evidence that these interactions are indeed driven by electrostatics, consistent with experiments. For example, the electrostatic repulsion between Cy5 and the 15% deprotonated surface is the strongest interaction measured in this study.

Development of synthesis protocols for Cy5 dye leading to minimal particle heterogeneity

In the last part we wanted to find out whether insights provided by the chromatographic assessment of C' dot heterogeneity could be used to develop synthetic protocols for Cy5 dye based C' dots, in particular targeting ligand functionalized c(RGDyC)-PEG-Cy5-C' dots, leading to minimal particle heterogeneity in surface chemical properties. Development of such protocols would be beneficial as they could keep changes to particle composition and

structure minimal relative to particles successfully employed in first FDA IND approved human clinical trials.[3] To that end, we identified a commercially available Cy5 dye derivative with positive net charge referred to as Cy5(+) and employed this compound in the regular synthesis of PEGylated (*i.e.* PEG-Cy5(+)-C' dot) as well as targeted (*i.e.* c(RGDyC)-PEG-Cy5(+)-C' dot) fluorescent core-shell silica NPs (see Methods section). Results of HPLC runs of these particles after batch purification steps *via* GPC are shown in Figure 6C (non-targeted C' dots) and 6D (targeted C' dots). For comparison, chromatograms of the original negatively charged Cy5 dye based equivalent particle products (compare to figure 1B blue line and figure 1C) are shown in the background of each panel 6C and 6D in light gray. As is evident from these comparisons, the homogeneity of both products has dramatically improved in that for both cases, the positively charged Cy5 dye derivative has resulted essentially in a single peak chromatogram. Furthermore, for both cases this peak is exactly on top of the peak of the negatively charged Cy5 dye product that has been identified as resulting from particles with Cy5 dye fully incorporated into the silica core of the C' dot. The differences that this dye placement induces in the PEG coating are illustrated for negatively charged and positively charged Cy5 dye in Figure 6A and B, respectively. While in the case of negatively charged Cy5 (6A) the dye has a large probability of ending up on the silica core surface, thereby leading to relatively hydrophobic surface patches that most likely are not PEGylated, in the case of the positively charged Cy5 derivative (6B) full dye encapsulation in the silica core leads to homogeneous PEG surface coverage, in turn resulting in single peak HPLC chromatograms. This picture is corroborated by zeta potential measurements on both particle batches (non-targeted C' dots) showing that the average zeta potential changed from slightly negative (–4.05 mV for PEG-Cy5-C' dots) to very close to zero (0.02 mV for PEG-Cy5(+) C' dots) when moving from the negatively to the positively charged Cy5 dye in the synthesis, consistent with expectations (see Supporting Information Figure S11). Finally, we performed coupled GPC-HPLC experiments with the untargeted positively charged Cy5 dye derivative (*i.e.* PEG-Cy5(+)-C' dot) as shown in Figure 3D. Working with fractions normalized in concentration to a very narrow range (Figure 3D, inset) they revealed no dependence of particle heterogeneity on size as corroborated by detailed comparison of different fractions as shown in Figure 3G. Comparison of waterfall plots for all three dots in Figure 3B, C, and D demonstrates the substantial improvement in particle batch surface chemical homogeneity achieved in this study.

Conclusions

In conclusion, in this study we introduce a combination of HPLC and GPC techniques to analyze heterogeneities of surface chemical properties of ultrasmall (<10 nm diameter) organic-inorganic hybrid core-shell nanoparticles and their correlation to particle size dispersity. Employing ultrasmall fluorescent core-shell silica NP assessments as an example, we demonstrate that these methods are very powerful revealing unexpected levels of surface chemical particle heterogeneities. Using a combination of various techniques, including molecular dynamics simulations, we show that these heterogeneities are due to different degrees of fluorescent dye encapsulation in the silica core, which in turn is governed by net dye compound charge. Using coupled GPC-HPLC runs we further show that the "worst case heterogeneity scenario" does not apply here, as different particle sizes separated *via* GPC

fractionation from a single particle synthesis batch do not lead to marked differences in surface chemical properties as revealed by HPLC. Finally, we demonstrate that insights provided by this chromatographic investigation leads to dramatically improved synthesis protocols for Cy5(+) dye encapsulating targeting ligand functionalized c(RGDyC)-PEG-Cy5(+)-C' dots, relative to particles derived from negatively charged Cy5 dye, that exhibit essentially a single HPLC peak suggesting full dye encapsulation and minimal heterogeneity of the resulting surface chemical properties, corroborated by essentially zero zeta potential of these particles. We expect that methods and insights provided by this study will be applicable to other ultrasmall organic ligand stabilized inorganic NPs thereby improving our understanding *e.g.* of NP structure-biological property correlations of such nanomaterials in applications including nanomedicine and oncology.

Materials & Methods

Materials

UHPLC grade acetonitrile was purchased from BDH. Superdex 200 resin was purchased from GE Healthcare Life Sciences. Vivaspin 30k MWCO spin filters were purchased from GE Healthcare Life Sciences. 5 M NaCl in water solution was purchased from Santa Cruz Biotechnology. Dimethyl sulfoxide (DMSO), Tetramethyl orthosilicate (TMOS), (3-Mercaptopropyl)trimethoxysilane (MPTMS), 2.0 M ammonia in ethanol were all purchased from Sigma-Aldrich. Methoxy-PEG(5–9)-silane (500g/mol) was purchased from Gelest. Cy5-maleimide, Cy5.5-maleimide, Cy3-maleimide were purchased from GE. TMR-maleimide (tetramethylrhodamine) purchased from Life Technologies. Alexa Fluor 647-COOH was purchased from Thermo Fisher. DI water generated using Millipore Milli-Q system (Milli-Q, 18.2 MΩcm). Atto647N-maleimide, Atto680-maleimide, and MB2-maleimide were purchased from Atto-Tec Gmbh. Xbridge Protein BEH C4 Column (300 Å, 3.5 μm, 4.6 mm X 150 mm, 10K-500K) and BioSuite. High Resolution SEC Column (250 Å, 5 μm, 7.8 mm X 300 mm, 10K – 500K) were purchased from Waters Technologies Corporation. Streptavidin and N-γ-maleimidobutyryl-oxysuccinimide ester (GMBS) were purchased from Life Technologies. TEM grids were copper coated with carbon film 300 mesh and were acquired from Electron Microscopy Sciences. Disposable zeta potential capillary cell was acquired from Malvern. All chemicals were used as received without further purification.

Particle Synthesis.

Cy5, TMR, Cy3, and Atto680 C' dots were synthesized as previously described[15]. Briefly, a mono functional maleimido derivatized dye was dissolved in DMSO overnight in a glovebox. A 25-fold excess of mercaptopropyltrimethoxysilane was added to the dissolved dye and allowed to react overnight in the glove box. The next day a flask containing deionized water adjusted to pH 8 using 2.0 M ammonia in ethanol solution was prepared and stirred vigorously. Tetramethylorthosilicate (TMOS) and the prepared dye-silane conjugate were added to the flask and allowed to react overnight. The following day, 100uL of mPEG(5–9)-silane was added to the flask and allowed to react overnight. The following day the stirring of the solution was stopped and the flask was heated to 80 C for 24 hours. Following this the particles are extensively dialyzed using 10k MWCO cellulose dialysis

tubing, followed by syringe filtration with a 200 nm membrane, spin filtering with a 30k MWCO PES membrane spin filter and finally GPC purification through Superdex 200 resin on a Bio-Rad FPLC. The particles are then characterized using fluorescence correlation spectroscopy on a home-built setup and UV/Vis spectroscopy on a Cary 5000 spectrometer. Atto647N and MB2 C' dots have a slight adjustment to the protocol, for a 10 mL reaction 2 mL of 0.02 M NH_4OH solution and 8 mL of DI water are added to the reaction flask instead of the previously reported 1 mL the resultant increase in pH was used to decrease the final size of the nanoparticles, as dyes with positive charges tend to form larger nanoparticles under standard conditions.

Gel Permeation Chromatography (GPC).

Preparative scale gel permeation chromatography was carried out on a Bio-Rad FPLC equipped with a UV detector set to 275 nm and a conductivity detector. Particles were purified in isocratic mode using 0.9 wt.% NaCl in deionized water. The solution was prepared at the time of purification by diluting 0.2 μm membrane filtered 5 M NaCl in water (Santa Cruz Biotechnology) with deionized water. The column used was hand-packed with Superdex 200 resin with dimensions 20 mm x 300 mm and run at a flow rate of 2.0 mL/min. All samples were concentrated in GE Life Sciences 30 kDa MWCO VivaSpin filters prior to injection the total injection volume was less than 1 mL per run. Particles eluted around the 15-minute mark and the total run lasted 30 minutes.

High Performance Liquid Chromatography (HPLC).

All injections were performed at a standardized injection volume and concentration. Concentrations for injected samples were determined prior to analysis by FCS. The columns used were 150 mm Waters Xbridge BEH C4 Protein separation columns with 300 Å pore size and 3.5 μm particle size. The separation method used is as follows: The sample was first injected onto the column in a flow of 90:10 water:acetonitrile at a flow rate of 1 mL/min. These conditions were maintained for 20 minutes to allow equilibration of the analyte with the stationary phase. After 20 minutes the flow rate was slowed to 0.5 mL/min and the baseline was allowed to equilibrate. Then the mobile phase composition was changed to 45:55 water:acetonitrile in a step-like fashion and the baseline was allowed to equilibrate again. Finally a composition gradient of 45:55 to 5:95 water:acetonitrile was carried out for 20 minutes, during this time the analyte elutes from the column. For additional details please see Supporting Information.

Steady-State Absorption Spectroscopy.

Absorbance spectra of particle samples and dye were measured in DI water on a Varian Cary 5000 spectrophotometer in a 3 mL quartz cuvette with a 10 mm light path (HellmaAnalytics) from 200 nm to 800 nm in 1 nm increments. All spectra were baseline corrected using a cuvette with DI water as reference cell. Peak intensities were kept between 0.01 and 0.06.

Single Particle Photobleaching Analysis.

To analyze the recorded movies *.zvi files were loaded into ImageJ and converted to 8-bit *.tiff files. Individual particle fluorescence time traces (arbitrary units, A.U.) were extracted using the custom software (ImageC.exe), developed and kindly provided by Dr. Warren Zipfel (Cornell University, NY, USA). Due to sparse labeling it was assumed that each point spread functions (PSF) in the image represents one particle. Particles were automatically located from the summed projection of the image stack by applying a Gaussian mask algorithm. Particle fluorescence time trace were the summed pixel intensities of 5×5 region of interest (ROI) centered around the brightest pixel and plotted against measurement time. The brightest pixel was maintained as the center of each ROI for each frame. Due to shot noise variations and possible minor drift, the ROI was allowed to move at most 1 pixel per frame. Fluorescence bleaching steps were counted by hand. Traces with undiscernable bleaching steps were rejected from the analysis. A total number of 644 particles were analyzed.

Fluorescence Correlation Spectroscopy (FCS).

All FCS measurements were carried out on a homebuilt confocal FCS setup. In short, a continuous wave laser beam (635 nm solid state laser for particle containing Cy5, ATTO647N, or ATTO680, and a 543 nm HeNe laser for particles containing TMR, or Cy3) is focused onto the image plane of a water immersion microscope objective (Zeiss Plan-Neofluar 63× NA 1.2). The stokes-shifted emitted fluorescence is collected by the same objective, passed through a dichroic mirror, spatially filtered by a 50 μm pinhole, split into two paths with a beam splitter, spectrally filtered by long pass filters (ET665lp, Chroma, for 635 nm excitation, and ET560lp, Chroma, for 543 nm excitation), and detected by two avalanche photodiode detectors (SPCM-AQR-14, PerkinElmer). To filter detector afterpulsing effects from sample fluorescence fluctuations, the detector signals were cross-correlated by a digital correlator (Flex03LQ, Correlator.com)[30], allowing lag time resolution of 15 ns. Respective correlation curves were fitted accounting for translational diffusion, photo-induced cis-trans isomerization, and rotational diffusion by using equation (1):

$$G(\tau) = 1 + \frac{1}{N_m}\left(\frac{1}{1 + \tau/\tau_D}\right)\left(\frac{1}{1 + \tau/(\tau_D\kappa^2)}\right)^{1/2}\frac{1}{(1-P)}\left(1 - P + P\exp(\tau/\tau_P)\right)\left(1 + \alpha_{Rot}\exp(\tau/\tau_{Rot})\right)$$

where N_m is the number of dye molecules or particles in the ellipsoidal observation volume, defined by a structure factor $\kappa = \omega_Z/\omega_{xy}$ with axial (ω_z) and radial (ω_{xy}) radii. τ_d is the average diffusion time of a dye or particle through the observation volume. P is the fraction of Cy5 dye molecules being in the non-fluorescent cis-conformation, which the characteristic relaxation time τ_p. For particles a third relaxation time is noticeable at very short lag times ($\tau = 100$ ns) that can be attributed to particle rotation, where α_{Rot} is the pre-exponential amplitude of particle rotation, and τ_{Rot} the characteristic rotational diffusion time of a particle. Particle rotation was not further characterized and only used for improved fits. All correlation curves were normalized according to equation (2):

$$G(\tau) = (G(\tau) - 1)N_m$$

For additional details please see Supporting Information.

Transmission electron microscopy measurements.

Samples were prepared by collecting the particles as they eluted from the HPLC and then casting the fractionated particles onto a carbon coated copper TEM grid. Briefly, 8 μL of the sample solution collected directly from the HPLC were dropped onto the TEM grid and then left in air to dry. Dry state transmission electron microscopy was carried out using a FEI Tecnai T12 Spirit microscope operated at 120 kV.

Simulations.

All-atom molecular dynamics (MD) simulations were performed using the AMBER 16 molecular dynamics package.[31] Initial coordinates as well as force field parameters for the amorphous silica surfaces were those published by Heinz *et al.*[32] All dye molecules were constructed in Discovery Studio Visualizer[33] and assigned force field parameters from the general AMBER force field (GAFF) version 1.8.[34] Dyes with attached silane units also included force field parameters from the CHARMM silicate force field published by Lopes *et al.*[35] applied to silicon and silicon− adjacent atoms. Partial charges were assigned to the dye molecules *via* the restrained electrostatic potential (R.E.S.P.) method using R.E.S.P. ESP charge Derive (R.E.D.) Server Development.[36] During R.E.S.P. calculations, the net molecule charge and the local charge on atoms shown with a formal charge were restrained. All dye molecules were individually energy minimized in vacuum prior to their addition to surface-solvent systems. The TIP3P water model[37] and monovalent ion parameters were employed as reported previously.[38]

Systems containing silica surfaces, dye, and water were constructed by first copying and translating the coordinates for an amorphous silica surface as previously described[32] to create a bonded silica surface approximately $80 \times 80 \times 20$ Å in the *x, y,* and *z* directions, respectively. Hydrogens were randomly removed to reach the desired deprotonation percentage, followed by changing the dangling oxygen atom types and partial charges as necessary. The target dye molecule was then added to the system with a center-of-mass 4–9 Å above the surface in the positive *z*-direction, with the distance chosen to ensure that the dye does not overlap with the silica surface after addition. The dye molecule was then randomly rotated by first choosing a random unit vector through the molecule center-of-mass as the axis of rotation and then a random angle between 0 and 2π by which to rotate the dye molecule. For each surface-dye combination, five independent systems differing only by this random dye molecule rotation were created and simulated. Reported linear interaction energies are the average of these five simulations. The dye molecule and silica surface were then solvated with TIP3P water using a buffer distance of 40 Å in the positive and negative *z*-directions. Random water molecules were then removed and replaced by positively-charged ammonium ions to reach a net neutral charge for the entire system. Thus, the starting simulation coordinates were approximately $80 \times 80 \times 130$ Å with 85,000–95,000

atoms total. Additional information, including simulation conditions and equilibration procedures are provided in the Supporting Information.

Zeta potential measurements.

Zeta potential measurements were carried out on a Malvern Zetasizer instrument operated at 20°C. Samples were inserted into a disposable capillary cell and after the samples were allowed to equilibrate 5 independent measurements were taken and then averaged to determine the zeta potential of each nanoparticle sample.

Supplementary Material

Refer to Web version on PubMed Central for supplementary material.

Acknowledgments

References:

1. Jadzinsky PD, Calero G, Ackerson CJ, Bushnell DA & Kornber RD Structure of a Thiol Monolayer-Protected Gold Nanoparticle at 1.1 A Resolution. Science 2007, 318, 430–433. [PubMed: 17947577]

2. Turner M; Golovko VB; Vaughan OPH; Abdulkin P; Berenguer-Murcia A; Tikhov MS; Johnson BFG; Lambert RM Selective Oxidation with Dioxygen by Gold Nanoparticle Catalysts Derived from 55-Atom Clusters. Nature 2008, 454, 981–983. [PubMed: 18719586]

3. Phillips E; Penate-Medina O; Zanzonico PB; Carvajal RD; Mohan P; Ye Y; Humm J; Gönen M; Kalaigian H; Schöder H; Strauss WH; Larson SM; Wiesner U; Bradbury MS Clinical Translation of an Ultrasmall Inorganic Optical-PET Imaging Nanoparticle Probe. Sci. Transl. Med. 2014, 6, 1–9.

4. Fenn JB, Mann M, Meng CKAI, Wong SF & Whitehouse CM Electrospray Ionization for Mass Spectrometry of Large Biomolecules. Science 1989, 246, 64–71. [PubMed: 2675315]

5. Lee S-W; Berger SJ; Martinovi S; Pasa-Toli L; Anderson GA; Shen Y; Zhao R; Smith RD Direct Mass Spectrometric Analysis of Intact Proteins of the Yeast Large Ribosomal Subunit Using Capillary LC/FTICR. Proc. Natl. Acad. Sci. U. S. A. 2002, 99, 5942–5947. [PubMed: 11983894]

6. Aebersold R & Mann M Mass Spectrometry-Based Proteomics. Nature 2003, 422, 198–207. [PubMed: 12634793]

7. Korevaar PA; George SJ; Markvoort AJ; Smulders MMJ; Hilbers PAJ; Schenning APHJ; De Greef TFA; Meijer EW Pathway Complexity in Supramolecular Polymerization. Nature 2012, 481, 492–496. [PubMed: 22258506]

8. Mullen DG; Fang M; Desai A; Baker JR; Orr BG; Banaszak-Holl MM A Quantitative Assessment of Nanoparticle-Ligand Distributions: Implications for Targeted Drug and Imaging Delivery in Dendrimer Conjugates. ACS Nano 2010, 4, 657–670. [PubMed: 20131876]

9. Howes PD, Chandrawati R & Stevens MM Colloidal Nanoparticles as Advanced Biological Sensors. Science 2014, 346,

10. Peer D; Karp JM; Hong S; Farokhzad OC; Margalit R; Langer R Nanocarriers as an Emerging Platform for Cancer Therapy. Nat. Nanotechnol. 2007, 2, 751–760. [PubMed: 18654426]

11. Nel AE; Mädler L; Velegol D; Xia T; Hoek EMV; Somasundaran P; Klaessig F; Castranova V; Thompson M Understanding Biophysicochemical Interactions at the Nano-Bio Interface. Nat. Mater. 2009, 8, 543–557. [PubMed: 19525947]

12. Volpi N & Linhardt RJ High-Performance Liquid Chromatography-Mass Spectrometry for Mapping and Sequencing Glycosaminoglycan-Derived Oligosaccharides. Nat. Protoc. 2010, 5, 993–1004. [PubMed: 20448545]

13. Ow H; Larson DR; Srivastava M; Baird BA; Webb WW; Wiesner U Bright and Stable Core-Shell Fluorescent Silica Nanoparticles. Nano Lett. 2005, 5, 113–117. [PubMed: 15792423]

14. Herz E, Ow H, Bonner D, Burns A & Wiesner U Dye Structure-Optical Property Correlations in Near-Infrared Fluorescent Core-Shell Silica Nanoparticles. J. Mater.Chem. 2009, 19, 6341–6347.

15. Ma K, Werner-Zwanziger U, Zwanziger J & Wiesner U Controlling Growth of Ultrasmall Sub-10 nm Fluorescent Mesoporous Silica Nanoparticles. Chem. Mater. 2013, 25, 677–691.

16. Ma K, Zhang D, Cong Y & Wiesner U Elucidating the Mechanism of Silica Nanoparticle PEGylation Processes Using Fluorescence Correlation Spectroscopies. Chem. Mater. 2016, 28, 1537–1545.

17. Ma K; Mendoza C; Hanson M; Werner-Zwanziger U; Zwanziger J; Wiesner U Control of Ultrasmall Sub-10 nm Ligand-Functionalized Fluorescent Core-Shell Silica Nanoparticle Growth in Water. Chem. Mater. 2015, 27, 4119–4133.

18. Yoo B, Ma K, Wiesner U & Bradbury M Expanding Analytical Tools for Characterizing Ultrasmall Silica-Based Nanoparticles. RSC Adv. 2017, 7, 16861–16865. [PubMed: 28944051]

19. Widengren J & Schwille P Characterization of Photoinduced Isomerization and Back-Isomerization of the Cyanine Dye Cy5 by Fluorescence Correlation Spectroscopy. J. Phys. Chem. A 2000, 104, 6416–6428.

20. Chmyrov V, Spielmann T, Hevekerl H & Widengren J Trans-Cis Isomerization of Lipophilic Dyes Probing Membrane Microviscosity in Biological Membranes and in Live Cells. Anal. Chem. 2015, 87, 5690–5697. [PubMed: 25927252]

21. Burns AA; Vider J; Ow H; Herz E; Penate-medina O; Baumgart M; Larson SM; Wiesner U; Bradbury M Fluorescent Silica Nanoparticles with Efficient Urinary Excretion for Nanomedicine. Nano Lett. 2009, 9, 442–448. [PubMed: 19099455]

22. Jain RK & Stylianopoulos T Delivering Nanomedicine to Solid Tumors. Nat. Rev. Clin. Oncol. 2010, 7, 653–664. [PubMed: 20838415]

23. Jiang W, Kim BYS, Rutka JT & Chan WCW Nanoparticle-Mediated Cellular Response is Size-Dependent. Nat. Nanotechnol. 2008, 3, 145–150. [PubMed: 18654486]

24. Kim HS, Farmer BL & Yingling YG Effect of Graphene Oxidation Rate on Adsorption of Poly-Thymine Single Stranded DNA. Adv. Mater. Interfaces 2017, 4, 1601168-1–1601168-9.

25. Peerless JS, Bowers GH, Kwansa AL & Yingling YG Effect of C60 Adducts on the Dynamic Structure of Aromatic Solvation Shells. Chem. Phys. Lett. 2017, 678, 79–84.

26. Zhao Y; Qi X; Ma J; Song L; Yang Y; Yang Q Interface of Polyimide−Silica Grafted with Different Silane Coupling Agents: Molecular Dynamic Simulation. J. Appl. Polym. Sci. 2018, 135,

27. Manning JRH, Yip TWS, Centi A, Jorge M & Patwardhan SV An Eco- Friendly, Tunable and Scalable Method for Producing Porous Functional Nanomaterials Designed Using Molecular Interactions. ChemSusChem 2017, 10, 1683–1691. [PubMed: 28235156]

28. Roscioni OM, Muccioli L, Mityashin A, Cornil J & Zannoni C Structural Characterization of Alkylsilane and Fluoroalkylsilane Self-Assembled Monolayers on SiO_2 by Molecular Dynamics Simulations. J. Phys. Chem. C 2016, 120, 14652–14662.

29. Cruz-Chu ER, Aksimentiev A & Schulten K Water-Silica Force Field for Simulating Nanodevices. J. Phys. Chem. B 2006, 110, 21497–21508. [PubMed: 17064100]

30. Widengren J, Rigler R & Mets U Triplet-State Monitoring by Fluorescence Correlation Spectroscopy. J. Fluoresc. 1994, 4, 255–258. [PubMed: 24233457]

31. Case DA; Cerutti DS; Cheatham TE, III; Darden TA; Duke RE; Giese TJ; Gohlke H; Goetz AW; Greene D; Homeyer N; Izadi S; Kovalenko A; Lee TS; LeGrand S; Li P; Lin C; Liu J; Luchko T; Luo R; Mermelstein D; et al. AMBER 2017. 2017.

32. Emami FS; Puddu V; Berry RJ; Varshney V; Patwardhan SV; Perry CC; Heinz H Force Field and a Surface Model Database for Silica to Simulate Interfacial Properties in Atomic Resolution. Chem. Mater. 2014, 26, 2647–2658.

33. Accelrys Software Inc. Discovery Studio Visualizer 4.0. 2013.

34. Wang J, Wolf RM, Caldwell JW, Kollman PA & Case DA Development and Testing of a General AMBER Force Field. J. Comput. Chem. 2004, 25, 1157–1174. [PubMed: 15116359]

35. Lopes PEM, Murashov V, Tazi M, Demchuk E & MacKerell AD Development of an Empirical Force Field for Silica. Application to the Quartz−Water Interface. J. Phys. Chem. B 2006, 110, 2782–2792. [PubMed: 16471886]

36. Vanquelef E; Simon S; Marquant G; Garcia E; Klimerak G; Delepine JC; Cieplak P; Dupradeau YFRED Server: a Web Service for Deriving RESP and ESP Charges and Building Force Field Libraries for New Molecules and Molecular Fragments. Nucl. Acids Res. 2011, 39, W511–W517. [PubMed: 21609950]

37. Jorgensen WL, Chandrasekhar J, Madura JD, Impey RW & Klein ML Comparison of Simple Potential Functions for Simulating Liquid Water. J. Chem. Phys. 1983, 79, 926–935.

38. Li P, Song LF & Merz KM Systematic Parameterization of Monovalent Ions Employing the Nonbonded Model. J. Chem. Theory Comput. 2015, 11, 1645–1657. [PubMed: 26574374]
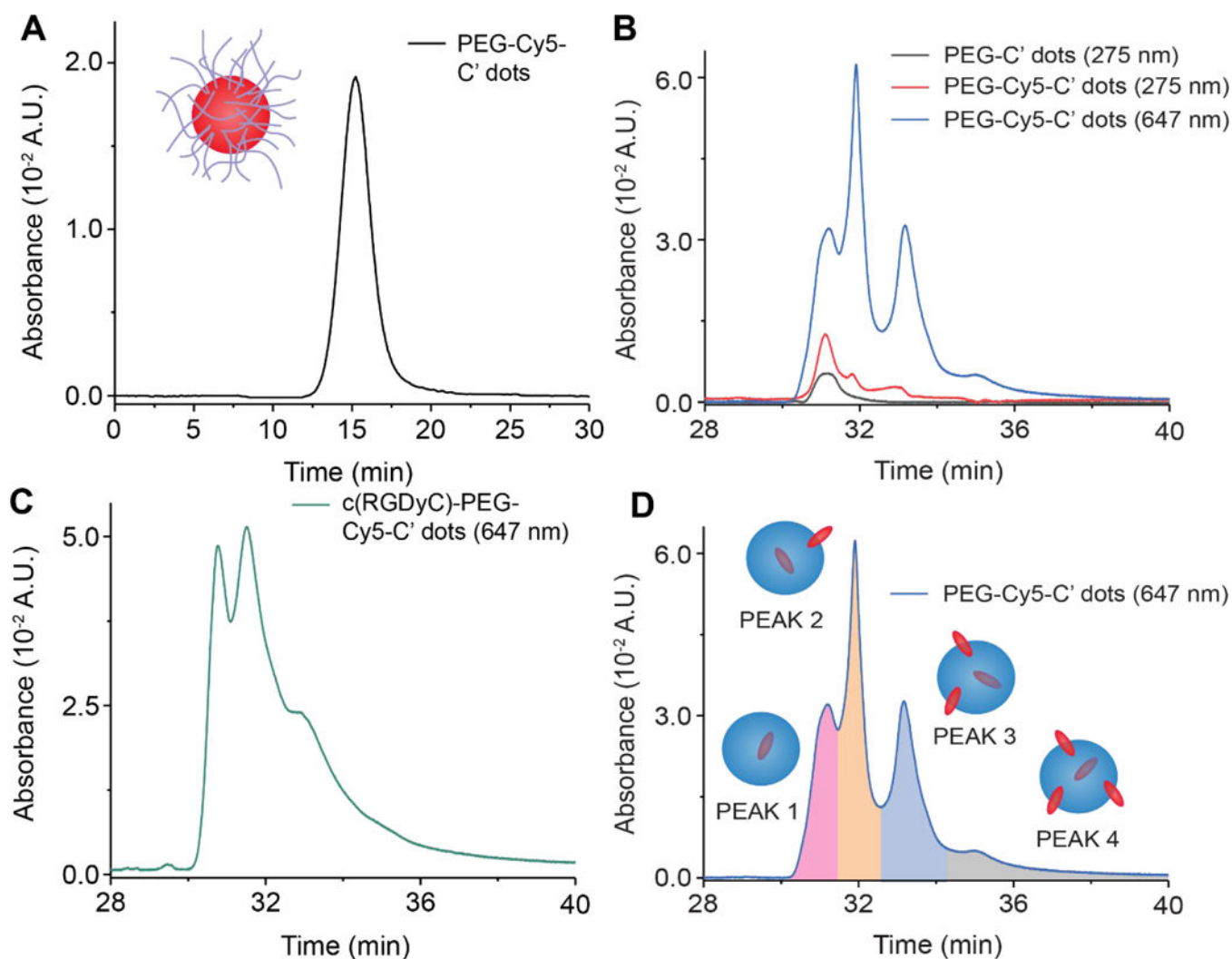
Fig. 1. Nanoparticle GPC and HPLC characterization.
(**A**) GPC of purified PEG-Cy5-C' dots recorded at 275 nm with particle illustration (inset).
(**B**) HPLC of PEG-Cy5-C' dots at 647nm (main) as well as of PEG-C' dots (black) and
PEG-Cy5-C' dots at 275 nm (red). (**C**) HPLC of c(RGDyC)-PEG-Cy5-C' dots at 647 nm.
(**D**) HPLC of PEG-Cy5-C' dots at 647 nm. Next to each of the four peaks is a schematic of
the suggested corresponding particle structure (blue circles) with dye locations (red ellipses).
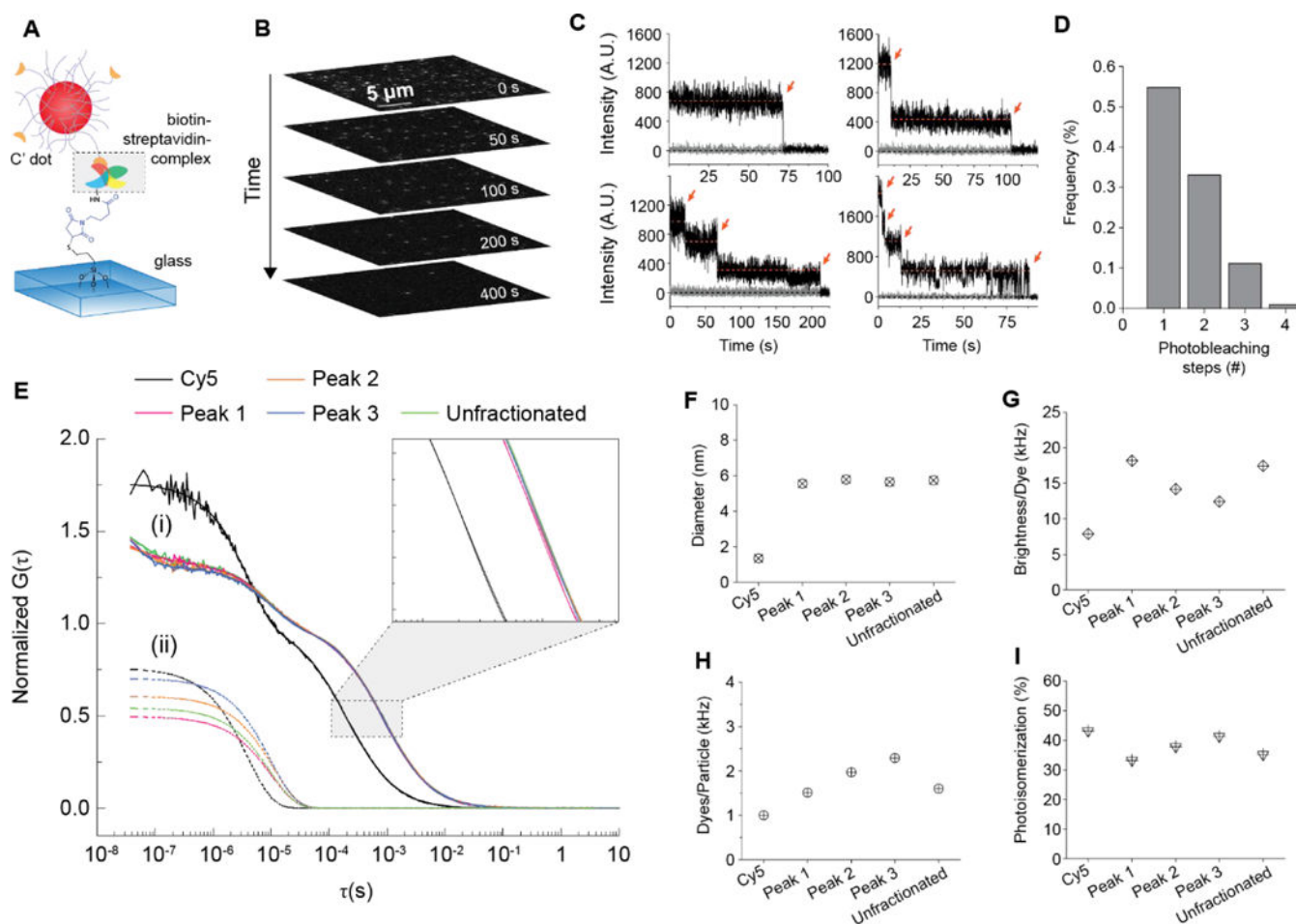
Fig. 2. Nanoparticle photobleaching and FCS.

(**A**) Schematic of a biotin functionalized PEGCy5-C' dot immobilized on a streptavidin coated glass slide for TIRFM. (**B**) Image stack of representative photobleaching time series. (**C**) Representative particle fluorescence intensity time traces from photobleaching. Red arrows indicate bleaching events. (**D**) Dye distribution in PEGCy5-C' dot batch derived from photobleaching. (**E**) (i) FCS correlation curves for free Cy5 dye and PEG-Cy5-C' dots under peaks 1–3 in Fig, 1C collected from successive HPLC runs. (ii)Individual contributions of cis-trans photoisomerization to respective FCS curves in (i). (**F**)Hydrodynamic diameter, (**G**) brightness per dye, (**H**) dyes per particle, and (**I**) photoisomerization percentage for free Cy5 dye as compared to PEG-Cy5-C' dots from HPLC fractionated peaks 1–3 in Fig. 1C.
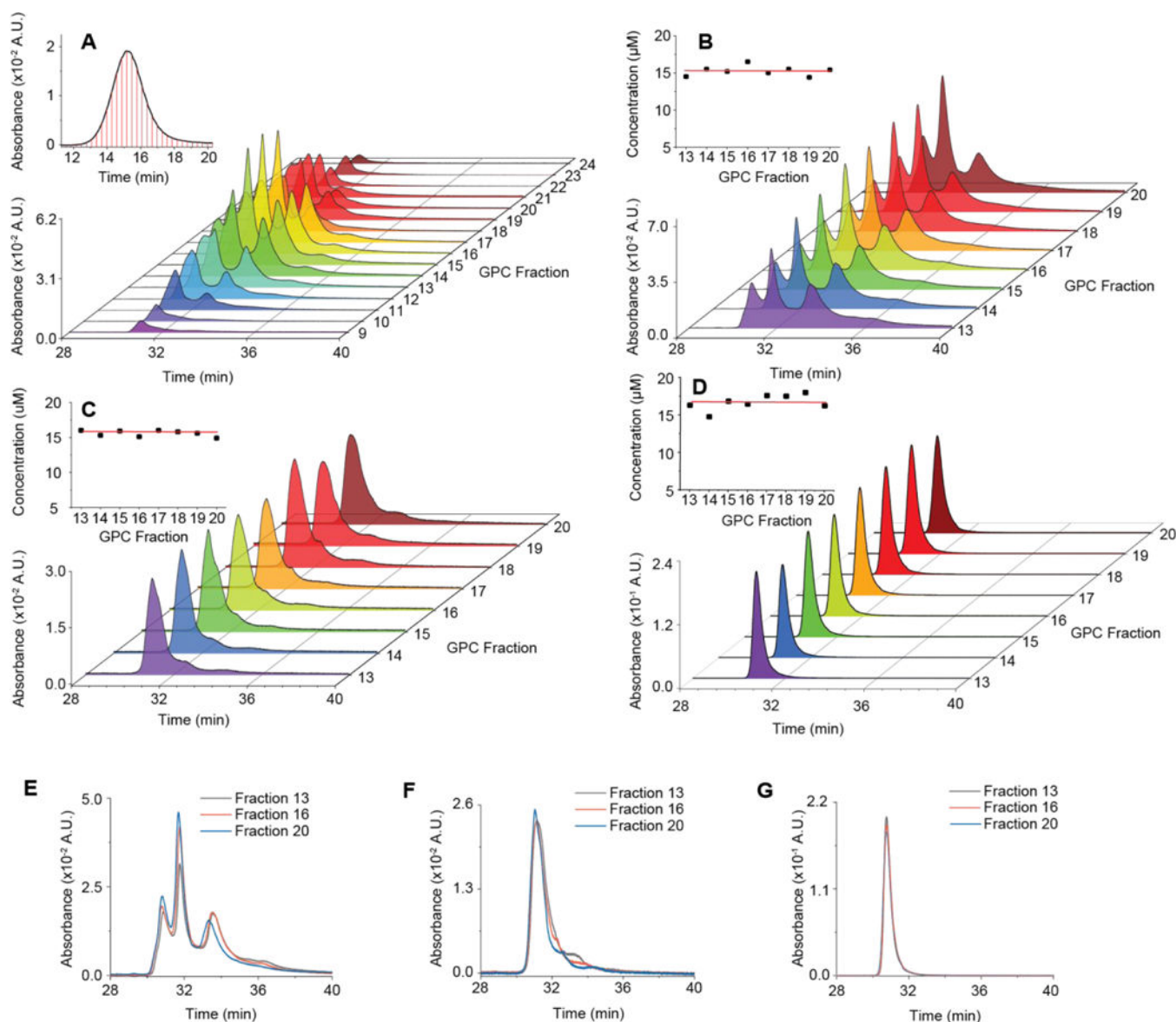
Fig. 3. Coupled GPC-HPLC nanoparticle characterization.

(**A**) Waterfall plot of coupled GPCHPLC runs for PEG-Cy5-C' dots. Inset shows GPC trace of PEG-Cy5-C' dots; red lines are the fraction collection starting points. (**B**) Waterfall plot of coupled GPC-HPLC runs for PEG-Cy5-C' dots from subset of GPC fractions collected in (A) and concentrated to a uniform concentration (inset) as determined by a combination of UV/Vis absorbance and FCS. (**C**) Same as in (B) for MB2 C' dots (PEG-MB2-C' dots), but with less uniform particle concentration, in part because methylene blue is a non-fluorescent dye, and FCS could not be performed. (**D**) Same as (B) and (C) but for PEG-Cy5(+)-C' dots, a particle synthesized using the same dye as in PEG-Cy5-C' dots, but with a net positive charge as opposed to a net negative charge. (**E,F,G**) Overlay of three representative chromatograms from concentration normalized coupled GPC-HPLC runs in (B), (C), and (D). Large (black), mid-sized (red), and small (blue) particles show minor (E,F) or no (G) differences in surface chemical heterogeneity, depending on particle type.
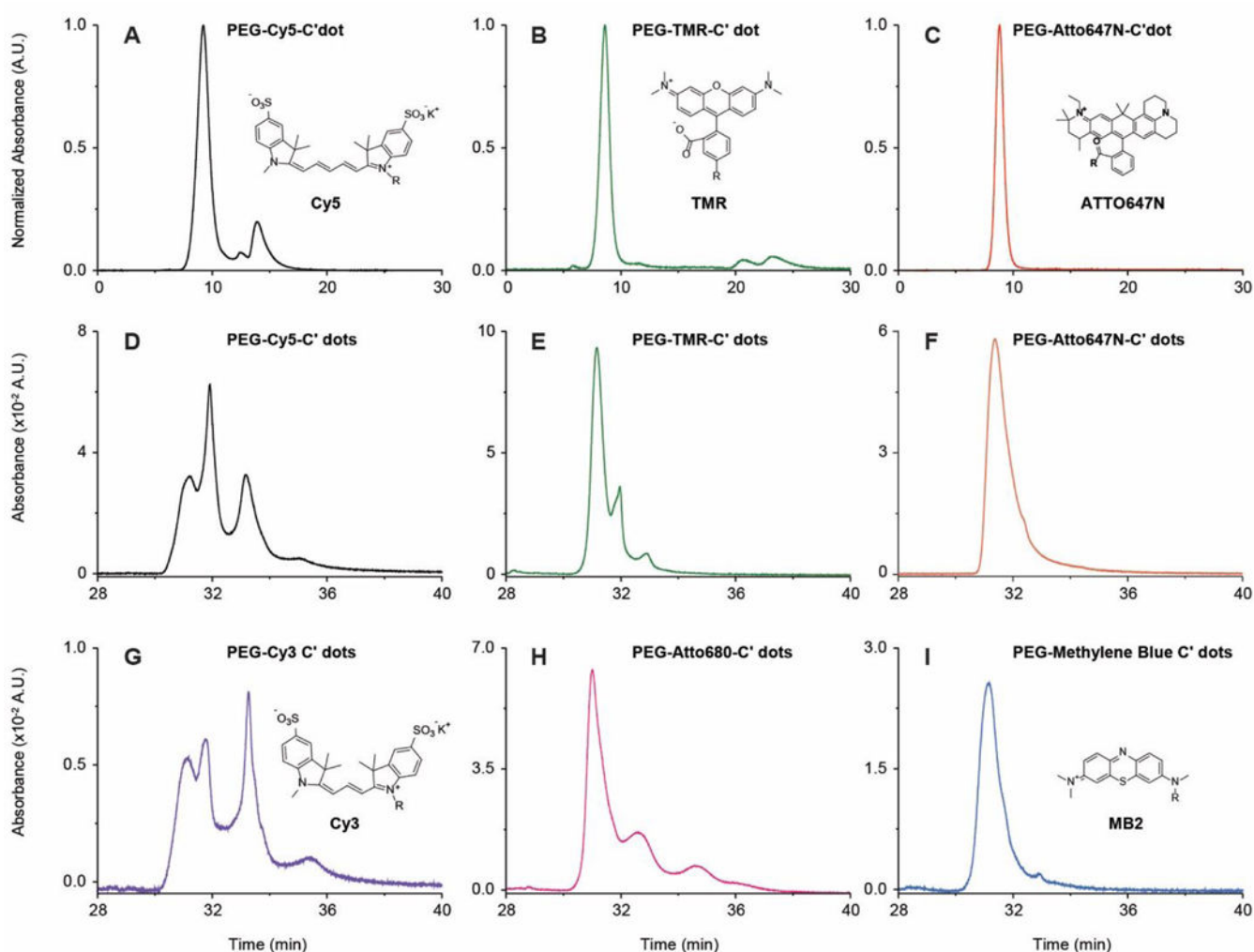
Fig. 4. Dye incorporation efficiency and nanoparticle heterogeneity as a function of dye charge.
(**A-C**) Analytical GPC chromatograms of native synthesis solutions prior to preparative scale purification: PEG-Cy5-C' dot solution (A) as detected at 647 nm with peaks corresponding to particles, PEG-Cy5 conjugates, and free Cy5, in order of elution (for incorporation efficiency, see SI Table S3); PEG-TMR-C' dot solution (B) as detected at 553 nm with largest peak corresponding to PEG-TMR-C' dots (for incorporation efficiency see SI Table S2); PEGATTO647N-C' dot solution (C) detected at 647 nm, (incorporation efficiency ~100%). (**D-I**) HPLC chromatograms of: PEG-Cy5-C' dots (D), PEG-TMR-C' dots (E), PEG-ATTO647N-C' dots (F), PEG-Cy3-C' dots (G), PEG-ATTO680-C' dots (H), and PEG-MB2-C' dots (I). Dye structures are shown in insets (the structure of ATTO680 is not available, but according to ATTOTec GmBH, the dye is zwitterionic).
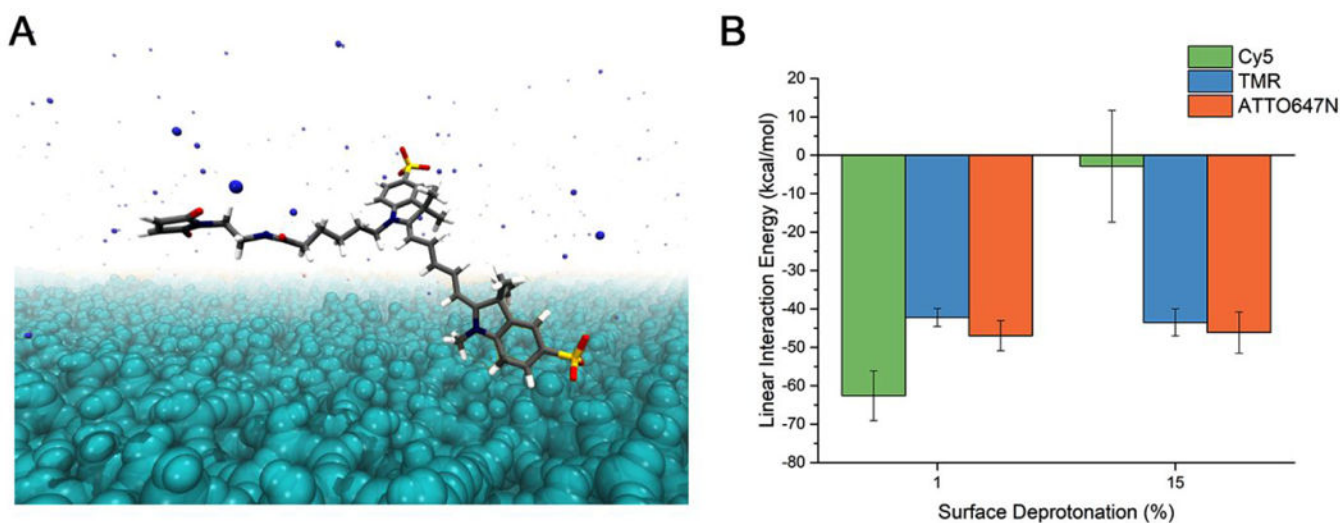
Fig. 5. Molecular dynamics (MD) simulations and analysis.
(**A**) Representative system setup of silica surface - dye MD simulations as-constructed, composed of water (not shown for clarity), amorphous SiO2 (cyan), Cy5 maleimide (carbon=gray, hydrogen=white, nitrogen=blue, oxygen=red, silicon=yellow), and ammonium ions (blue spheres). In other systems Cy5 maleimide is replaced with the dye of interest. (**B**) Total linear interaction energies calculated between silica surfaces and dye silane molecules. Reported values are the average of the last 20 ns of five 100 ns simulations with randomly-oriented initial dye coordinates (see Materials & Methods for more details).
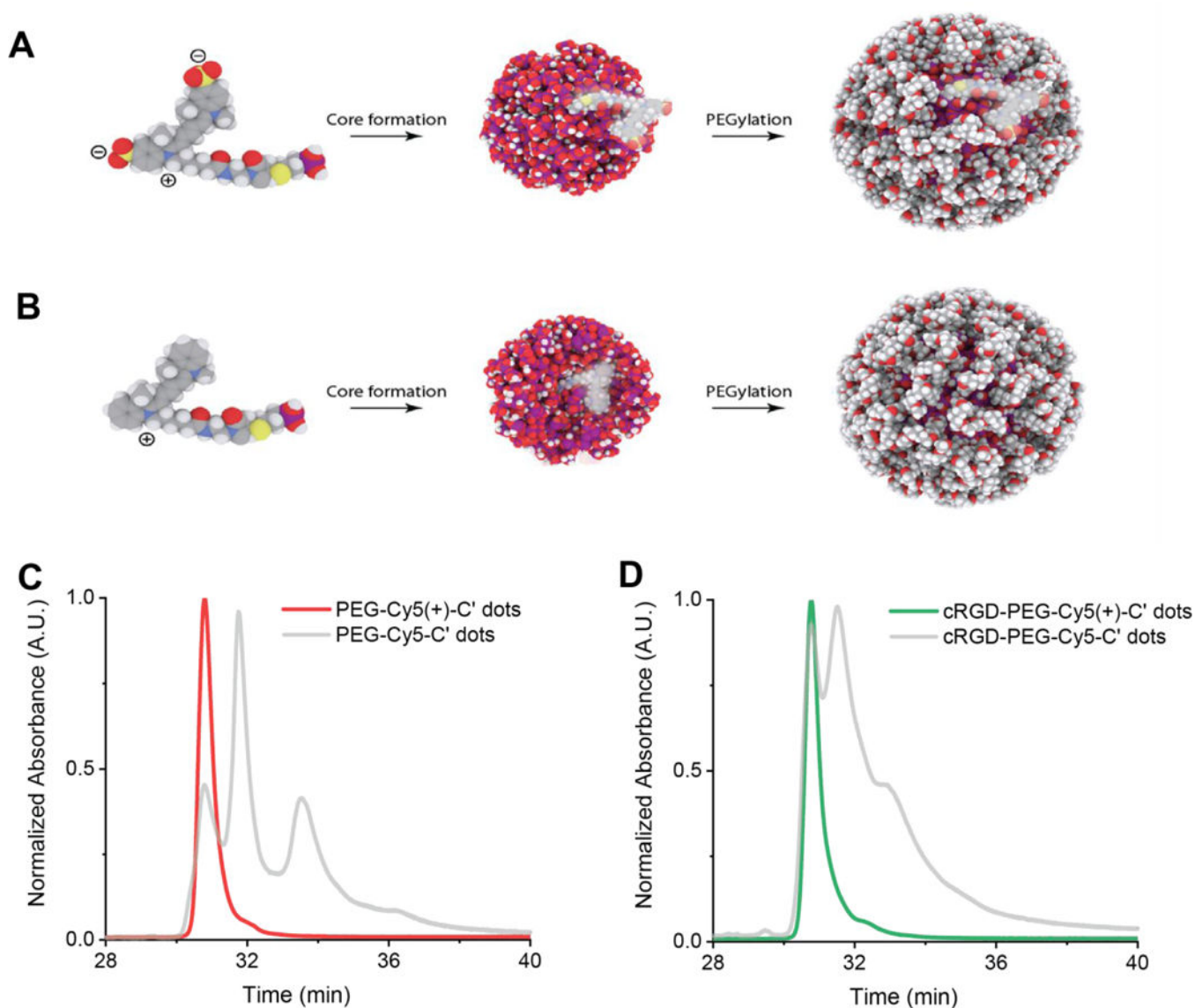
Fig. 6. HPLC results from positively charged Cy5 dye derived C' dots.
(**A**) Representative schematic of silica particle core structure and associated negatively charged Cy5 dye (left side) location on surface (middle) leaving un-PEGylated patches on the final particle surface after PEGylation (right side). (**B**) Schematic of silica particle core structure with associated positively charged Cy5 dye (left side) location within the silica core (middle), leading to homogeneously surface patches. (**C**) HPLC chromatogram of PEG-Cy5(+)-C' dots (red) as compared to same particle derived from negatively charged Cy5 dye (gray). (**D**) HPLC chromatogram of targeting ligand functionalized c(RGDyC)-PEG-Cy5(+)-C' dots (green) as compared to same particle derived from negatively charged Cy5 dye (gray).